Journal of Energy Storage 182 (2026) 125019

Contents lists available at ScienceDirect

Journal of Energy Storage

journal homepage: www.elsevier.com/locate/est

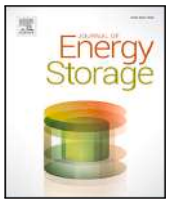

Research Papers

Impact of mechanical stress on electrochemical performance of the lithium-ion battery

Jasmina Tabaković, Tomaž Katrašnik, Klemen Zelič *

University of Ljubljana, Faculty of Mechanical Engineering, Laboratory for Internal Combustion Engines and Electromobility, Aškerčeva 6, Ljubljana, 1000, Slovenia

ARTICLE INFO

Keywords:
Lithium-ion battery (LIB)
Doyle–Fuller–Newman (DFN)
Mechanical stress
Electrochemical impedance spectroscopy (EIS)
Distribution of relaxation times (DRT)
Incremental capacity analysis (ICA)

ABSTRACT

Mechanical stress plays a critical role in the performance and degradation of lithium-ion batteries, yet their coupling with electrochemical processes remains insufficiently explored. This work investigates these interactions by fully coupling the Doyle–Fuller–Newman (DFN) model within the PyBaMM framework with a mechanical sub-model at both particle and electrode scales that accounts for both concentration-driven and interaction-driven stress contributions. The developed framework enables the consistent simulation of incremental capacity analysis (ICA), electrochemical impedance spectra (EIS), and distribution of relaxation times (DRT) under applied mechanical pressure. ICA reveals mechanical loading shifts voltage-capacity peaks, reflecting stress-induced changes in reaction equilibria. EIS complements this by showing voltage-dependent impedance evolution, with DRT spectra exhibiting changes in peak intensity and characteristic times.

Using a fundamental thermodynamic framework based on Gibbs free energy minimization, we demonstrate that these shifts originate from a stress-induced modification of the chemical potential. Importantly, we show that full-cell behavior is governed by the predominant electrode, where the competition between material properties (E_p, ν, Ω) and the open-circuit potential (OCP) slope determines the direction of voltage and impedance shifts. This framework provides a consistent physical explanation for non-monotonic impedance trends and resolves seemingly contradictory findings in previous literature, identifying the specific conditions under which mechanical stress either enhances or hinders electrochemical kinetics.

1. Introduction

The rising demand for efficient, reliable energy storage in portable electronics, residential systems, and electric vehicles has established lithium-ion batteries (LIBs) as a leading technology, valued for their high energy density, long cycle life, and favorable power characteristics. However, their performance and longevity are limited by complex, coupled degradation mechanisms that are difficult to observe directly. Accurate prediction of these processes is essential for improving performance, enhancing safety, and extending service life — ultimately enabling better state-of-health diagnostics and reducing lifecycle costs.

While experimental studies remain indispensable, many of these degradation phenomena occur on scales or under conditions that are challenging to capture in the laboratory. This has driven the growing use of numerical simulations based on physics-driven electrochemical models [1–4], which represent the fundamental physical and chemical processes that govern cell behavior. Such models provide fast, cost-effective, and non-invasive access to the battery's internal dynamics, and they enable systematic parametric studies that would be impractical experimentally, making them a powerful complement to empirical research.

Alongside electrochemical factors, mechanical stress significantly influences the internal state and degradation of lithium-ion cells [5]. Such stress arises from substantial volumetric changes in electrode particles during lithium insertion and extraction, as well as from external stack or casing constraints. It alters transport coefficients, perturbs interfacial reaction kinetics, and promotes microstructural damage, such as particle cracking and loss of electrical contact [6–8]. Since these effects are mechanically driven and tightly coupled to lithium transport and reaction kinetics, they are best captured with fully coupled electrochemical–mechanical models.

Existing mechanical models [9,10] typically assume that each electrode particle is isolated, with mechanical stress fields arising solely from volume expansion or contraction during lithiation. This assumption neglects stresses generated by particle–particle interactions, despite studies showing that such interaction-induced stresses are non-negligible [11,12] and comparable in magnitude to those caused by concentration gradients [13,14]. Addressing this limitation, this work adopts a multiscale electrochemical–mechanical model of Bin and Wei [15], that consistently couples mechanical and electrochemical

* Corresponding author.
E-mail address: klemen.zelic@fs.uni-lj.si (K. Zelič).

https://doi.org/10.1016/j.est.2026.125019
Received 10 June 2026; Received in revised form 15 September 2026; Accepted 29 September 2026
Available online 9 October 2026
2352-152X/© 2026 The Authors. Published by Elsevier Ltd. This is an open access article under the CC BY-NC-ND license (http://creativecommons.org/licenses/by-nc-nd/4.0/).

behavior from the particle scale to the continuum, thereby enabling detailed investigation of how mechanical stress influences electrochemical responses in LIB.

These responses are often characterized using non-invasive diagnostic techniques such as incremental capacity analysis (ICA) and electrochemical impedance spectroscopy (EIS), the latter frequently analyzed further via distribution of relaxation times (DRT) to deconvolve overlapping electrochemical processes. EIS is one of the most widely used non-invasive methods for characterizing electrochemical systems, including lithium-ion batteries. It resolves the system's voltage-current response into its frequency components by applying a small-amplitude sinusoidal voltage or current perturbation, typically ±5–10 mV or ±5% of the nominal current, over a broad frequency range extending from kHz down to mHz.

This frequency-dependent impedance enables separation of processes occurring at distinct frequencies, including charge-transfer reactions, ionic diffusion, and electrolyte transport [16].

In this context, EIS provides a frequency-resolved view of the cell response, while DRT analysis [17] further decomposes the impedance by solving an ill-posed inverse problem that yields a continuous distribution of relaxation processes associated with the mentioned electrochemical phenomena, thereby revealing their characteristic timescales.

Building on this frequency-domain perspective, ICA provides a complementary voltage-domain perspective by examining the derivative of capacity with respect to voltage, dQ/dV. This analysis is sensitive to electrochemical signatures associated with structural and interfacial changes in the electrodes; therefore, shifts in the position, width, and amplitude of characteristic peaks can be used to assess how mechanical stress alters the voltage-capacity relationship of the cell.

Despite the extensive use of EIS, DRT, and ICA for battery diagnostics, several important aspects of the electrochemical–mechanical coupling in lithium-ion cells remain insufficiently understood. Most studies employ these methods to characterize electrochemical dynamics [18–21], predicting state of charge (SoC) and state of health (SoH) [22–28], or identifying degradation mechanisms [29–33], without explicitly resolving stress effects. Although numerous studies have investigated the influence of mechanical stress on electrochemical impedance, the existing body of work is almost exclusively experimental and the reported trends are not consistent. Some authors have observed that increasing mechanical pressure reduces cell impedance [34–38], whereas others have reported that higher pressure impedes interfacial kinetics and mass transport, thereby increasing cell impedance [39–43], indicating that the underlying mechanisms are not fully elucidated. This is further corroborated by Drießen et al. [44], who observed a non-monotonic dependence of impedance on preload force in commercial NMC/graphite pouch cells, suggesting that the impedance response to mechanical loading is state- and load-dependent. Moreover, several studies have restricted their analysis to the low-frequency Warburg tail of the impedance spectrum, limiting the insight into pressure-induced changes across the full frequency range [45,46].

Existing DRT studies of mechanically loaded cells rely exclusively on experimental impedance spectra, covering solid-state batteries, symmetric cells and large prismatic cells [47–51]. However, these works do not clarify how pressure reshapes DRT features at different operating voltages, and the lack of physics-based, model-generated DRT insights limits quantitative interpretation of how individual relaxation processes respond to external pressure.

To the authors' knowledge, there are also no reports using ICA to directly analyze electrochemical–mechanical coupling in lithium-ion batteries. The closest related work is by Samad et al. [52], who introduced an incremental capacity analysis based on force (ICF) that replaces voltage with a mechanical signal and demonstrated that bulk compression and preload can be used to track capacity fade from dQ/dF peaks in constrained NMC prismatic cells, but without resolving how externally applied pressure modifies the underlying electrochemical processes reflected in ICA features. Together, these divergent and often partial findings highlight the lack of a unified, physics-based framework that quantifies how external pressure modifies the fundamental electrochemical behavior of lithium-ion cells across operating conditions.

To address this gap, this work presents the first numerical investigation of mechanical stress effects on the electrochemical response of lithium-ion battery through ICA, EIS, and DRT simulations, providing quantitative insight into how stress fields modify diffusion kinetics, interfacial reactions, and cell performance over a range of operating conditions. The simulations are performed with a fully coupled electrochemical–mechanical framework for lithium-ion batteries implemented in the open-source PyBaMM platform, where the classical Doyle–Fuller–Newman (DFN) electrochemical model is extended by a multiscale mechanical sub-model that links particle- and electrode-level behavior and accounts for both concentration-driven and interaction-driven stress. This integrated approach not only establishes a new modeling capability for systematically studying coupled electrochemical–mechanical phenomena in lithium-ion cells, but also reveals for the first time that the seemingly contradictory trends reported in the experimental literature arise from an electrode-dominance mechanism: the direction and magnitude of stress-induced shifts in ICA, EIS, and DRT signatures are governed by the competition between the mechanical properties and the OCP slope of the two electrodes, with the predominant electrode dictating the full-cell response. Grounded in Gibbs free energy minimization, this thermodynamic framework provides a unified physical explanation for non-monotonic impedance behavior across different materials, cell designs, and states of charge, thus resolving a long-standing ambiguity in the experimental literature.

2. Multi-scale model

Lithium-ion battery operation is governed by strongly coupled processes spanning multiple scales, from lithium transport within active particles to charge and stress evolution at the electrode level. While the classical DFN model provides a rigorous electrochemical description across particle and electrode domains, it does not account for the feedback of mechanical stresses on transport and kinetics. In this work, the DFN framework in PyBaMM is extended with a fully coupled electrochemical–mechanical formulation, enabling a consistent description of interactions between particle- and electrode-scale phenomena.

2.1. Electrochemical model

The electrochemical behavior of the cell is modeled using porous electrode theory, formulated in the pseudo-two-dimensional (P2D) framework, commonly referred to as the DFN model [2]. This model captures battery behavior across two coupled scales: the macroscopic electrode scale and the microscopic particle scale. At the macroscopic scale, it resolves the solid-phase potential ϕ_s, electrolyte potential ϕ_e, and electrolyte lithium-ion concentration c_e along the cell thickness in the x-direction, with $y-z$ directions homogenized. At the microscopic scale, it models radial diffusion of lithium within spherical electrode particles, expressed as $c_s(r)$, with reactions occurring only at the particle surface. The two scales are coupled through electrochemical kinetics at the particle-electrolyte interface.

The DFN model is governed by mass and charge conservation equations in both phases. Eq. (1) describes intercalated lithium transport in solid particles via Fickian diffusion in spherical geometry, while Eq. (5) governs electronic charge distribution via Ohm's law. In the electrolyte phase, mass conservation (Eq. (10)) accounts for both diffusion and migration of Li^+ ions, while charge conservation (Eq. (14)) incorporates ionic conductivity and the effects of concentration gradients. These two phases are coupled via the total molar pore wall flux J_{TOT}, which integrates Butler-Volmer electrochemical kinetics (Eq. (17)) and double-layer capacitive effects (Eq. (18)). This interfacial flux is driven

Table 1
Governing equations and boundary conditions in a P2D model [2].

P2D model

Electrode

Mass Conservation (solid)

$$\frac{\partial c_{s,i}}{\partial t} = \frac{1}{r^2}\frac{\partial}{\partial r}\left(r^2 D_{s,i}\frac{\partial c_{s,i}}{\partial r}\right); \quad i \in \{p,n\} \tag{1}$$

$$\text{Initial condition: } c_{s,i} = c_{s,i,0} \tag{2}$$

Boundary conditions:

$$\left.\frac{\partial c_{s,i}}{\partial r}\right|_{r=0} = 0, \tag{3}$$

$$\left.-D_{s,i}\frac{\partial c_{s,i}}{\partial r}\right|_{r=R_s} = J_i \tag{4}$$

Charge conservation (solid)

$$\sigma_{\text{eff},i}\frac{\partial^2 \phi_{s,i}}{\partial x^2} = a_i F J_i^{\text{TOT}}(x,t); \quad i \in \{p,n\} \tag{5}$$

$$\left.-\sigma_{\text{eff,p}}\frac{\partial \phi_p}{\partial x}\right|_{x=0} = I_{\text{app}}, \tag{6}$$

$$\left.-\sigma_{\text{eff,n}}\frac{\partial \phi_n}{\partial x}\right|_{x=L} = I_{\text{app}}, \tag{7}$$

$$\left.-\sigma_{\text{eff,p}}\frac{\partial \phi_p}{\partial x}\right|_{x=L_p} = 0, \tag{8}$$

$$\left.-\sigma_{\text{eff,n}}\frac{\partial \phi_n}{\partial x}\right|_{x=L_p+L_s} = 0 \tag{9}$$

Electrolyte

Mass conservation (electrolyte)

$$\frac{\partial c_{e,i}}{\partial t} = \frac{1}{\varepsilon_i}\frac{\partial}{\partial x}\left(D_{e,i}^{\text{eff}}\frac{\partial c_{e,i}}{\partial x}\right) + \frac{\left(1-t_+^0\right)a_i J_i^{\text{TOT}}(x,t)}{\varepsilon_i}; \tag{10}$$

$$\text{Initial condition: } c_{e,i} = c_{e0} \quad i \in \{p,s,n\} \tag{11}$$

Boundary conditions:

$$\left.-D_{e,n}\frac{\partial c_{e,n}}{\partial x}\right|_{x=0} = 0, \tag{12}$$

$$\left.-D_{e,p}\frac{\partial c_{e,p}}{\partial x}\right|_{x=L} = 0 \tag{13}$$

Charge conservation (electrolyte)

$$-\frac{\partial}{\partial x}\left(\kappa_{e,i}\frac{\partial \phi_{e,i}}{\partial x}\right) + \beta\frac{\partial}{\partial x}\left(\frac{\kappa_{e,i}}{c_{e,i}}\frac{\partial c_{e,i}}{\partial x}\right) = a_i F J_i^{\text{TOT}}(x,t); \tag{14}$$

$$i \in \{p,s,n\}$$

$$\left.-\kappa_{e,p}\frac{\partial \phi_{e,p}}{\partial x}\right|_{x=0} = 0, \tag{15}$$

$$\left.-\kappa_{e,n}\frac{\partial \phi_{e,n}}{\partial x}\right|_{x=L} = 0 \tag{16}$$

Pore wall flux

Butler-Volmer equation

$$J^{\text{BV}} = \begin{cases} \frac{j_0}{F}\left[\exp\left(-\frac{F\alpha}{R_g T}\eta\right) - \exp\left(\frac{F(1-\alpha)}{R_g T}\eta\right)\right], & i \in \{p,n\}, \\ 0, & i = s, \end{cases} \tag{17}$$

Double layer equation

$$J^{\text{DL}} = \frac{\tilde{C}_{\text{DL}}}{F}\frac{\partial\left(\phi_s - \phi_e\right)}{\partial t} \tag{18}$$

Exchange current density

$$j_0 = k\sqrt{c_e\, c_{s,\text{surf},i}\left(c_{s,\max,i} - c_{s,\text{surf},i}\right)}, \quad i \in \{p,n\}, \tag{19}$$

Total molar flux

$$J^{\text{DL}} + J^{\text{BV}} = J^{\text{TOT}} \tag{20}$$

Overpotential

$$\eta = \phi_{s,i} - \phi_{e,i} - E_{\text{ref}}, \quad i \in \{p,n\} \tag{21}$$

by the local surface overpotential η, defined in Eq. (21) as the difference between the solid and electrolyte potentials, adjusted by the concentration-dependent open-circuit voltage U_{OCV}.

The governing equations are listed in Table 1 and implemented within the PyBaMM framework [53]. Numerical solutions are obtained using the finite volume method at both scales, with electrode-separator interfaces treated by harmonic averaging to ensure numerical stability.

2.2. Mechanical model

Lithium intercalation and deintercalation cause active material particles to expand and contract, generating mechanical stress field that can ultimately lead to particle fracture and capacity fade. To capture these effects, the P2D electrochemical framework is extended with a two-scale mechanical model representing both the macroscopic (electrode) and microscopic (particle) scales, where the active material particles are idealized as identical, isotropic, linear-elastic spheres undergoing small deformations. The governing equations and boundary conditions for this framework are summarized in Table 2.

At the macroscopic scale, the electrode is treated as a continuum in mechanical equilibrium (Eq. (24)), where the macroscopic stress Σ_{ij} arises from the effective elastic response to the volumetric strain e_0 driven by changes in the average lithium concentration $c_{s,\text{avg}}$ (Eq. (22)). At the microscopic scale, mechanical equilibrium (Eq. (26)) of a particle is maintained under the assumption of symmetry at the center and a traction-free surface (Eqs. (27) and (28)).

The constitutive relations (Eqs. (29) and (30)) couple linear elasticity with chemical expansion via the partial molar volume Ω, which is thereby an important coupling parameter that determines the strain produced by the local concentration deviation $\tilde{c}$. These relations, combined with compatibility equations (Eqs. (31) and (32)), yield analytical solutions for radial, tangential, and hydrostatic stresses within the particle (Eqs. (33)–(35)), introduced by Zhang et al. [9].

The resulting hydrostatic stress at the particle surface, $\sigma_{\text{h,surf}}$ (Eq. (38)), serves as the primary coupling variable that modulates the electrochemical potential and charge-transfer kinetics. Following the continuum-particle coupling described by Bin and Wu [15], this variable accounts for both the local concentration-induced stress σ_h^{c} (Eq. (35)) and the macroscopic interaction-induced stress $\langle\sigma_{ij}^{\text{i}}\rangle_{\text{s}}$ (Eq. (25)). The latter represents the stress generated by particle-to-particle interactions within the electrode assembly, thereby bridging the micro- and macroscopic scales.

2.3. Electrochemical-mechanical coupling methodology

The mechanical and electrochemical domains are coupled bidirectionally: concentration gradients drive particle volume changes, producing stresses that lower the local chemical potential and, in turn, influence interfacial reaction kinetics and lithium transport. To capture these effects, the DFN model was extended with stress-dependent terms, enabling a fully coupled electrochemical–mechanical description.

Table 2
Governing equations and boundary conditions in a mechanical model.

Mechanical model			
Continuum scale			
Macroscopic stress		**Mechanical equilibrium**	
$\Sigma_{ij} = C^H_{ijkl}\left(e_{kl} - e_0\delta_{kl}\right)$,	(22)	$\nabla \cdot \Sigma = \mathbf{0}$	(24)
$e_0 = \frac{\Omega^H}{3}\left(c_{s,avg} - c_{s0}\right)$	(23)		
Interaction induced stress [15]			
$\Sigma_{ij} = f_s\langle\sigma^i_{ij}\rangle_s$	(25)		
Particle scale			
Mechanical equilibrium		Boundary conditions:	
$\frac{d\sigma^c_{rr}}{dr} + \frac{2}{r}\left(\sigma^c_{rr} - \sigma^c_{\theta\theta}\right) = 0$	(26)	$u\vert_{r=0} = 0,$	(27)
		$\sigma^c_{rr}\vert_{r=R_i} = 0$	(28)
Constitutive equation		**Compatibility equation**	
$\varepsilon^c_{rr} = \frac{1}{E_p}\left(\sigma^c_{rr} - 2\nu_p\,\sigma^c_{\theta\theta}\right) + \frac{\Omega}{3}\tilde{c},$	(29)	$\varepsilon^c_{rr} = \frac{du}{dr},$	(31)
$\varepsilon^c_{\theta\theta} = \frac{1}{E_p}\left(\sigma^c_{\theta\theta} - \nu_p\left(\sigma^c_{\theta\theta} + \sigma^c_{rr}\right)\right) + \frac{\Omega}{3}\tilde{c}$	(30)	$\varepsilon^c_{\theta\theta} = \frac{u}{r}$	(32)
Radial, tangential and hydrostatic stress [9]		**Displacement**	
$\sigma^c_{rr}(r) = \frac{2\Omega E_p}{3\left(1-\nu_p\right)}\left(\frac{1}{R_i^3}\int_0^{R_i}\tilde{c}r^2dr - \frac{1}{r^3}\int_0^{r}\tilde{c}r^2dr\right)$	(33)	$u^c\left(R_i\right) = \frac{\Omega R_i}{3}\left(c_{s,avg} - c_{s0}\right),$	(36)
$\sigma^c_{\theta\theta}(r) = \frac{\Omega E_p}{3\left(1-\nu_p\right)}\left(\frac{2}{R_i^3}\int_0^{R_i}\tilde{c}r^2dr + \frac{1}{r^3}\int_0^{r}\tilde{c}r^2dr - \tilde{c}\right)$	(34)	$c_{s,avg} = \frac{3}{R_i^3}\int_0^{R_i} c_s(r)r^2dr$	(37)
$\sigma^c_h(r) = \frac{\sigma^c_{rr} + 2\sigma^c_{\theta\theta}}{3} = \frac{2\Omega E_p}{3\left(1-\nu_p\right)}\left(\frac{1}{R_i^3}\int_0^{R_i}\tilde{c}r^2dr - \frac{\tilde{c}}{3}\right)$	(35)		
Hydrostatic stress on a particle surface			
$\sigma_{h,surf} = \sigma^c_h\left(R_i\right) + \left\langle\sigma^i_h\right\rangle_s$	(38)		

The stress effect on diffusion was introduced via the equivalent diffusion coefficient proposed by Chu and Lee [54]:

$$D_{eq}(r) = D_s\left(1 + \frac{2\,\Omega^2 E_p c_s}{9R_gT(1-\nu)}\right), \tag{39}$$

where D_s is the solid diffusion coefficient, Ω the partial molar volume of lithium, E_p the Young's modulus of the active material, c_s the solid-phase lithium concentration, R_g the universal gas constant, T the temperature, and ν the Poisson's ratio.

Lithium flux in the solid phase is driven by gradients in chemical potential. Under the assumptions of small elastic strains and concentration-independent mechanical properties, the chemical potential in an active particle can be expressed as [55,56]:

$$\mu = \mu_c(c_s) - \Omega\sigma_h, \tag{40}$$

where $\mu_c(c_s)$ denotes the chemical potential in the stress-free state, and σ_h represents the hydrostatic stress in the particle.

Consequently, the reaction overpotential was reformulated to account for the stress-dependent shift in chemical potential as [15]:

$$\eta_m = \Phi_s - \Phi_e - E_{ref}(c_{s,surf}) - \frac{\Omega\sigma_{h,surf}}{F}. \tag{41}$$

where Φ_s and Φ_e are the solid and electrolyte potentials, E_{ref} is the reference open-circuit potential, $\sigma_{h,surf}$ the surface hydrostatic stress, and F Faraday's constant.

Finally, the local current density was reformulated through a stress-augmented Butler-Volmer expression [15]:

$$J = \frac{j_0}{F}\exp\left[\frac{(\alpha_m - \alpha)\,\Omega\sigma_{h,surf}}{R_gT}\right]\left[\exp\left(-\frac{F\alpha}{R_gT}\eta_m\right) - \exp\left(\frac{F(1-\alpha)}{R_gT}\eta_m\right)\right], \tag{42}$$

where j_0 is the exchange current density, α the charge-transfer coefficient, and α_m its stress-modified counterpart.

The integration of Eqs. (39), (41), and (42) establishes a robust bidirectional coupling between the mechanical stress fields and the electrochemical transport and kinetics within the DFN framework. In this formulation, the partial molar volume Ω and the surface hydrostatic stress $\sigma_{h,surf}$ serve as the important coupling parameters that map mechanical strain onto the electrochemical response of the cell. By incorporating these stress-dependent terms into the PyBaMM environment, the model coherently accounts for both particle-scale expansion and electrode-scale interactions, providing a physically consistent description of the interplay between mechanical deformation and electrochemical behavior, as illustrated in Fig. 1. It should be noted, however, that this study isolates this thermodynamic and kinetic coupling pathway from other mechanically induced effects, such as compression-induced changes in porosity and tortuosity, which affect electrolyte transport. Given the strongly interconnected nature of electrochemical–mechanical coupling, isolating this pathway provides a controlled basis for identifying its specific signature in the ICA, EIS, and DRT response, independent of concurrent transport-property changes.

2.4. Material properties

The material properties used in this study are summarized in Table 3. Electrochemical parameters were sourced from the PyBaMM dataset based on Mohtat et al. [57], having been validated against graphite/NMC pouch cell data. Mechanical properties for the NMC cathode were obtained from the experimental characterization by Cheng et al. [58], while the graphite anode parameters were sourced from Laresgoiti et al. [59], where they were validated within a mechanical degradation model against experimental cycle-life data.

3. Electrochemical diagnostic techniques: ICA, EIS, and DRT

To assess the influence of mechanical stresses on the electrochemical behavior of the cell, a hydrostatic stress in the range of 1 and

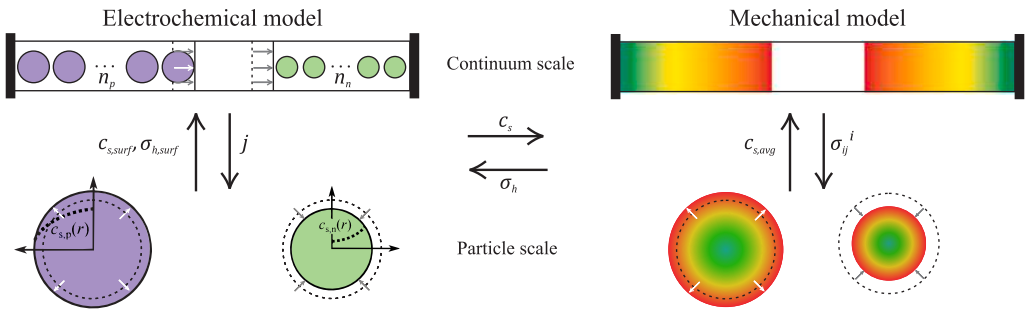

Fig. 1. Bidirectional coupling of stress fields and electrochemical processes on particle- and electrode-scale in the DFN framework.

Table 3
List of model parameters for graphite/NMC pouch cell [57].

Parameter	Cathode (NMC)	Separator	Anode (graphite)
Thickness L_i [μm]	67	12	62
Particle radius R_i [μm]	3.5	–	2.5
Active material fraction ε_s [–]	0.445	–	0.610
Porosity ε_e [–]	0.3	0.4	0.3
Bruggeman's coefficient *brugg* [–]	–	1.5	–
Maximum concentration $c_{s,max}$ [mol m^{-3}]	35 380	–	28 746
Reaction rate constant k [mol m^{-2} s^{-1} (mol m^{-3})$^{-1.5}$]	$5.0{\cdot}10^{-11}$	–	$1.1{\cdot}10^{-11}$
Electrode conductivity σ [S m^{-1}]	100	–	100
Double layer capacity $\tilde{C}_{DL}$ [F m^{-2}]	0.2	–	0.2
Charge transfer coefficient α [–]	0.5	–	0.5
Stoichiometric coefficients [SoC = 1] [–]	0.033	–	0.8332
Stoichiometric coefficients [SoC = 0] [–]	0.890	–	0.002
Solid diffusivity D_s [m^2 s^{-1}]	$8{\cdot}10^{-15}$	–	$5{\cdot}10^{-15}$
Young's modulus E_p [GPa]	199 [58]	–	15 [59]
Poisson's ratio ν [–]	0.25 [58]	–	0.3 [59]
Partial molar volume Ω [cm^3 mol^{-1}]	$1.25{\cdot}10^{-5}$		$3.1{\cdot}10^{-6}$ [59]
		Electrolyte	
Initial electrolyte concentration c_e [mol m^{-3}]		1000	
Electrolyte diffusion coefficient D_e		$5.2{\cdot}10^{-21}$	
Electrolyte conductivity κ [S m^{-1}]		1.3	
Transference number t_+ [–]		0.38	
Parameter for the whole cell			
Total electrode area [m^2]		0.2050	
Cell density ρ_{cell} [g cm^{-3}]		3100	

10 MPa range was applied to the coupled electrochemical–mechanical model described in Section 2. This pressure range was selected to encompass both the internal pressures observed in commercial cells and the broader range of external stack pressures (0–10 MPa) applied to industrial battery modules to maintain structural integrity [40,60,61]. A smaller pressure range was not selected here, as the resulting voltage and impedance changes would be less apparent, though similar trends are expected (Eqs. (40)–(42)). The simulated voltage response at different pressure levels was then used to compute the incremental capacity curves, electrochemical impedance spectrum, and distribution of relaxation times (see Appendix A for the corresponding equations).

Incremental capacity analysis was performed to evaluate how mechanical stress modifies the voltage-capacity relationship of the cell. Simulations were carried out at three hydrostatic stress levels during both charge (up to 4.2 V) and discharge (down to 3.0 V) at C/100. The resulting dQ/dV curves were smoothed using a Savitzky–Golay filter [62] and plotted as a function of voltage. All ICA curves were compared in a single figure to identify stress-induced shifts in peak position, providing qualitative evidence of how mechanical loading modifies the equilibrium potential of the electrode reactions.

Subsequently, electrochemical impedance spectroscopy was employed to investigate how mechanical stress field affects the full impedance spectrum, thereby enabling quantitative comparison of stress-induced changes in diffusion kinetics and charge-transfer current distribution. To estimate the impedance spectrum, a computational workflow was implemented in Python. First, a set of excitation frequencies in the kHz–mHz range was generated on a logarithmic scale and, for each frequency, a sinusoidal current signal was applied to the full DFN electrochemical model with mechanical coupling. The model was solved over a time window spanning several cycles of the applied perturbation, and the simulated voltage response was fitted with a sinusoidal function to obtain the amplitude, phase shift, and mean voltage. From these fitted parameters, the real and imaginary parts of the impedance were computed and assembled into a frequency-dependent spectrum, which was subsequently presented in a Nyquist plot.

Finally, distribution of relaxation times analysis was used to deconvolute and quantify the contributions of individual processes – such as diffusion and charge-transfer kinetics – that cannot be directly separated from the total cell impedance in a Nyquist plot. In this work, the commercial RelaxIS DRT software [63], based on the framework developed by the Ciucci group [64], was employed. Instead of conventional Voigt elements, the DRT function is discretized using radial basis functions (RBFs), which provide a smooth representation of the impedance over the relaxation-time spectrum. The DRT was deconvolved from the high- to mid-frequency semicircular region of the impedance spectrum, using a Gaussian radial basis function with a first-order differentiation matrix penalizing the derivative of $\gamma(\ln \tau)$ and a regularization parameter of $\lambda = 10^{-3}$ (Tikhonov regularization). Resulting spectra were represented as $\gamma(\tau)$ versus τ, with the characteristic relaxation time τ (s) plotted on a logarithmic time axis and $\gamma(\tau)$ on the ordinate as a dimensionless measure of the relative contribution of processes relaxing at each τ. The relative RMSE between reconstructed

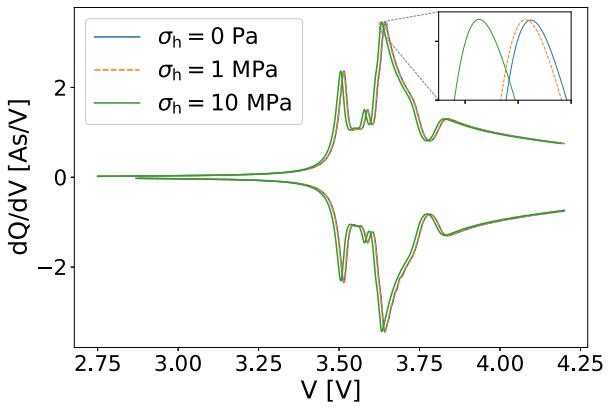

Fig. 2. Incremental capacity analysis at three different hydrostatic stress levels, illustrating the influence of stress fields on the equilibrium potential of the electrode reactions.

and simulated impedance spectra remained low across all conditions (0.64%–0.75%), confirming good DRT fit quality independent of stress level or state of charge.

4. Results and discussion

The results of the coupled electrochemical–mechanical simulations are presented in three parts. First, IC curves are used to track stress-induced changes in electrochemical activity through shifts in peak positions. Second, Nyquist plots are analyzed to demonstrate how applied mechanical stress reshapes the impedance spectra, with particular emphasis on charge-transfer processes. Finally, DRT analysis is employed to resolve overlapping electrochemical processes contained within the EIS response.

Fig. 2 shows the incremental capacity (dQ/dV) curves obtained at three different hydrostatic stress levels during both charge (positive values) and discharge (negative values). The distinct peaks correspond to characteristic electrochemical processes occurring within the electrodes; therefore, variations in their position, height, and width serve as sensitive indicators of how mechanical stress influences cell behavior.

The ICA simulation results reveal that mechanical stress induces a systematic shift of all peaks toward lower voltages. This effect is particularly pronounced at a stress level of 10 MPa but remains noticeable even at 1 MPa. The shift can be directly attributed to the mechanical contribution to the lithium chemical potential (Eq. (40)), where hydrostatic stress lowers the equilibrium chemical potential of the electrode reactions. Consequently, the voltage regions associated with the highest electrochemical activity, identified by the peaks in the dQ/dV curves, are displaced. However, the observation that all peaks in the full cell shift toward lower voltages (Fig. 2) is not immediately obvious and requires further explanation.

The underlying mechanism can be understood through basic thermodynamics. The Gibbs free energy density of intercalated lithium in an active particle (G), which drives the electrochemical reaction, can be expressed as:

$$G = H - TS + Ue - \frac{1}{2}\int \sigma : \epsilon \, dV \tag{43}$$

Here, H represents the bonding enthalpy of lithium within the electrode, TS is the entropy contribution, Ue denotes the electric potential energy associated with the intercalated charge, and the last term accounts for the mechanical stress contribution to the Gibbs free energy. By subtracting the Gibbs free energy of the electrolyte, one obtains the Gibbs free energy difference that drives the electrochemical reaction. Differentiating this difference with respect to the number of intercalated lithium ions yields the chemical potential difference. For completeness, a condensed derivation, adapted from [15,65], is provided in Appendix B.

At equilibrium, the chemical potential difference must vanish, leading to:

$$\boldsymbol{\Phi}_s - \boldsymbol{\Phi}_e - E_{\text{ref}} - \frac{\Omega\,\sigma_h}{F} = 0 \tag{44}$$

This expression corresponds to the overpotential defined in Eq. (41). Each term can be directly linked to Eq. (43): E_{ref} represents the equilibrium potential derived from the combined enthalpy and entropy contributions (Nernst equation), $\boldsymbol{\Phi}_s - \boldsymbol{\Phi}_e$ is the potential difference between the electrolyte and the solid (linked to Ue), and the final term, $\frac{\Omega\,\sigma_h}{F}$, arises from the mechanical stress energy contribution.

Eqs. (43) and (44) clearly explain the origin of the dQ/dV peak shifts. Introducing stress moves the system out of equilibrium, and Gibbs free energy minimization drives the system back by adjusting the voltage (via the Ue term in Eq. (43) or $\boldsymbol{\Phi}_s - \boldsymbol{\Phi}_e$ in Eq. (44)). This adjustment manifests as an apparent reduction of the equilibrium potential of both electrodes due to mechanical strain - a phenomenon known as the stress dependence of the chemical potential, recently measured in silicon half-cells [65]. Consistent with these measurements, Eq. (44) implies that the equilibrium electric potential at an individual electrode interface increases under compressive stress when referenced to Li/Li^+. This single-electrode shift originates directly from the mechanical term in Eq. (43), as the free-energy perturbation scales with the partial molar volume Ω.

However, in a full-cell configuration, directly translating the single-electrode formulations in Eqs. (43) and (44) is not straightforward, as mechanical effects occur simultaneously at both electrodes. While the equilibrium potentials of both electrodes increase when referenced to Li/Li^+, the measured full-cell voltage reflects the difference between these potentials. The stress-induced shift of the full-cell response is therefore governed not by the mechanical term of either electrode individually, but by the difference between the two mechanical contributions, so that the peaks in the full-cell dQ/dV response may shift either to lower or higher voltages, depending on which electrode dominates the mechanical response. The dominant contribution is governed by the material parameters E_p, ν, and Ω defined in Eqs. (22)–(41). Because Ω is nearly an order of magnitude larger for the cathode than for the anode (Table 3), the cathode contribution dominates and the full-cell peaks shift toward lower voltages. This interpretation is further supported by two figures in the Appendix C. First, the galvanostatic discharge curves in Fig. C.5 exhibit a distinct downward baseline shift under mechanical loading, confirming a reduction in operating cell voltage and altered interfacial overpotentials. Second, the internal battery states depicted in Fig. C.6 show that, in accordance with Eq. (44), applied compressive stress decreases the cathode solid potential and increases both the electrolyte concentration and electrolyte potential, while the anode solid potential remains unchanged due to the 0 V Dirichlet boundary condition.

EIS and DRT simulations reveal additional insights. Fig. 3 shows the results of the EIS simulations for the NMC/graphite cell under three applied pressures and at three operating voltages. The voltages of 3.64 V, 3.72 V, and 3.98 V correspond to 30%, 50%, and 80% SoC, respectively, for the uncompressed cell. The Nyquist plots reveal that mechanical pressure significantly alters the cell's impedance response, as evident from the variation in the size and shape of the semicircles in the high- to medium-frequency range and from the modified slope of the Warburg-type tail at low frequencies. The corresponding differences in Re(Z) and Im(Z) relative to the unstressed baseline, shown as a function of frequency directly below each Nyquist plot in Fig. 3, further quantify these stress-induced shifts across the measured frequency range.

Since the simulations are based on the standard DFN model, no electrical contact is modeled. Consequently, no parallel shift to lower real impedance is observed, as sometimes reported under stress [40]. However, this approach allows us to isolate the mechanical stress impact on the charge-transfer resistance semicircle in EIS, which arises

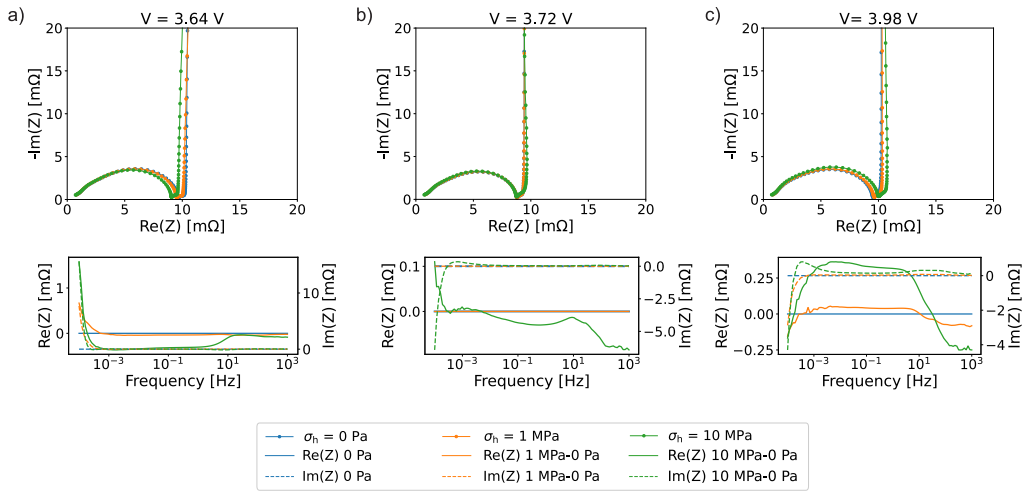

Fig. 3. Nyquist plots (top row) and corresponding differences in real and imaginary impedance components relative to the unstressed baseline as a function of frequency (bottom row) at operating voltages of (a) 3.64 V, (b) 3.72 V, and (c) 3.98 V under three different stress fields, showing the voltage dependence of stress-induced changes in cell's impedance.

from electrochemical–mechanical coupling rather than the electrical domain. Analogously to dQ/dV peak shifts, stress-induced changes in impedance spectra originate from shifts in electrochemical equilibrium potential caused by the mechanical contribution to the lithium chemical potential (Eq. (40)).

For EIS, a constant voltage is enforced, as the experiment is valid only when the system is at equilibrium at a fixed potential. Voltages of 3.64 V, 3.72 V, and 3.98 V, corresponding to 30%, 50%, and 80% SoC, were chosen for the simulated battery. Under applied mechanical stress and fixed voltage, the voltage contribution in Gibbs free energy (Eq. (43)) cannot compensate for the mechanical energy, so the system cannot relax via voltage adjustment. Instead, the particle stoichiometry – the amount of intercalated charge – adapts to the applied stress (charge e in Eq. (43)). Compressive stress promotes lithium deintercalation at constant voltage, whereas tensile stress favors intercalation. In other words: under open-circuit conditions, applying mechanical stress to the cell shifts the measured voltage, whereas under the potentiostatic conditions used here, the voltage is fixed by definition, and the system instead exchanges charge with the external circuit, so its stoichiometry adjusts in response to the applied stress. Importantly, this effect arises from the influence of strain on reaction thermodynamics rather than from direct volume changes of the particles.

In full-cell operation, the predominant electrode again determines the response, but in this case the dominance depends not only on E_p, ν, and Ω, but also strongly on the slope of the open-circuit potential with respect to stoichiometry, which governs the voltage-charge relationship. The influence of these parameters on the impedance response is examined systematically in Appendix D, where Ω and D_{eq} were varied for each electrode individually to test electrode dominance, and the cathode OCP slope was varied to assess generalizability across chemistries. As shown below, in the present chemistry case the cathode is the predominant electrode. Robustness to cell geometry was additionally verified by simulating a cell with 1.5×the baseline electrode thickness, which reproduced the same qualitative trends.

Mechanical stress tends to increase lithium stoichiometry in both electrodes. At equilibrium under constant voltage, the full-cell state of charge adjusts such that the stoichiometry of the dominant electrode decreases while that of the other increases. By definition, an increase in the overall cell state of charge corresponds to lithium transfer from the cathode to the anode — that is, a decrease in cathode stoichiometry and an increase in anode stoichiometry. The observed increase in overall state of charge under applied pressure therefore identifies the cathode as the electrode whose stoichiometry decreases, confirming that the cathode is the dominant electrode in Figs. 3 and 4. This small shift in state of charge leads to observable changes in the EIS and DRT spectra because the charge-transfer resistance is stoichiometry dependent. Specifically, the charge-transfer resistance decreases with pressure at 3.64 V, remains nearly unchanged at 3.72 V, and increases at 3.98 V.

These trends arise because the charge-transfer resistance is inversely proportional to the exchange current density (Eq. (19)), which is a non-monotonic function of surface stoichiometry. Stress-induced changes in stoichiometry modify the exchange current density, leading to either an increase or a decrease in charge-transfer resistance depending on state of charge. The magnitude and sign of this change are governed by the slope of $j_0(c_{s,surf})$ in Eq. (19). At low surface concentrations, the slope of j_0 is positive, resulting in reduced charge-transfer resistance under applied pressure, as observed in Fig. 3. At high surface concentrations, the slope becomes negative, leading to increased resistance. Around intermediate stoichiometries (approximately 50% SoC), the slope is close to zero, and the charge-transfer resistance remains largely unaffected by mechanical stress. This behavior is directly reflected in Fig. E.9 (Appendix E), which shows the stress-induced variation in cathode solid-phase surface concentration across the examined voltage levels.

In contrast to the Nyquist plots, which reflect the overall impedance response across different frequency regions, the DRT representation enables separation of overlapping electrochemical processes and direct inspection of their pressure-dependent evolution. Fig. 4 shows that three dominant processes govern the impedance response, each associated with a distinct relaxation time. These peaks correspond to ohmic, charge-transfer, and double-layer contributions at high to intermediate frequencies, as well as diffusion-related processes at lower frequencies. With increasing mechanical pressure, both the positions and amplitudes of these peaks evolve, indicating systematic changes in reaction kinetics and mass transport pathways.

Building on Rüther et al. [66], the three DRT peaks can be interpreted physically based on their characteristic timescales. Peak 1 (10^{-3} s) is associated with fast cathode charge-transfer and double-layer processes, Peak 2 (10^{-2} s) with the slower anode charge-transfer and double-layer response, consistent with the higher cathode reaction rate constant in the present parametrization (Table 3) and with the faster

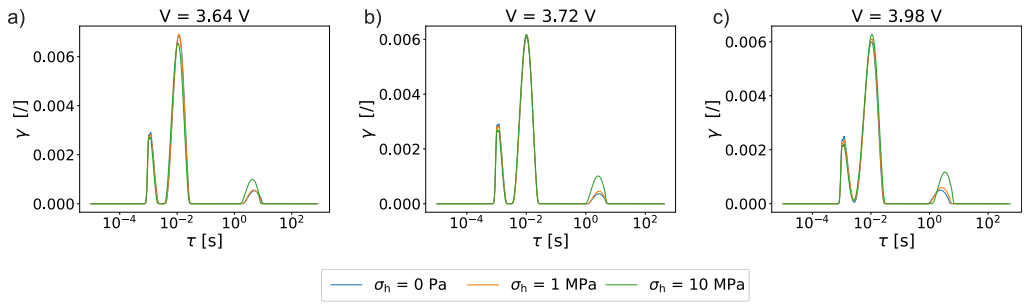

Fig. 4. DRT analysis at operating voltages of (a) 3.64 V, (b) 3.72 V, and (c) 3.98 V under three different stress fields, showing the voltage dependence of stress-induced changes in the cell's electrochemical response.

cathode charge-transfer timescales reported by Rüther et al. This assignment is further confirmed by the electrode-specific parametric sweep in Fig. D.8, where increasing the cathode partial molar volume Ω_p selectively increases Peak 1, while increasing the anode partial molar volume Ω_n selectively increases Peak 2. The close agreement between the summed area of Peaks 1 and 2 and the charge-transfer resistance obtained directly from the Nyquist semicircle (Appendix F) confirms that these two peaks, unlike the artifactual Peak 3 discussed below, represent genuine electrochemical processes rather than deconvolution artifacts.

The high-timescale feature (Peak 3, 10^1 s) coincides with the upper bound of the resolvable timescale range, where RBF-based DRT deconvolution bounds the estimated distribution even though the true DRT should diverge as the impedance diverges at low frequency [67]. Peak 3 therefore originates from the discretization basis rather than from a physical relaxation process. This distinction matters beyond the present dataset, as peaks at large timescales are commonly reported in DRT analyses of battery impedance data and attributed to electrolyte diffusion or mass transport, when they may in fact be artifacts of the same kind. Accordingly, Peak 3 is not assigned a physical interpretation here, and the electrode-dominance analysis below relies exclusively on Peaks 1 and 2.

The pressure dependence of the peaks reflects how each electrode responds to stress. Peak 1 decreases with increasing pressure at all voltages, indicating reduced cathode charge-transfer resistance. This is explained by pressure-driven changes in cathode stoichiometry toward values that maximize exchange current density; the effect is strongest at low SoC and weaker, though still present, at high SoC where stoichiometric changes are more constrained.

Peak 2 captures the anode response and shows opposite trends depending on SoC. At low SoC, pressure increases anode stoichiometry in a regime where exchange current rises, reducing resistance. At high SoC, the same shift moves the anode into a regime where exchange current decreases, increasing resistance. This reversal matches the behavior of the mid-frequency EIS feature.

This framework provides a consistent explanation for the seemingly contradictory trends reported in the literature. Both the choice of active materials, which determines the predominant electrode, and the state-of-charge dependence of stress effects play a crucial role. Consequently, measurements performed at different states of charge may yield opposing trends even for nominally identical cells.

5. Conclusions

In this work, we have developed a fully coupled electrochemical–mechanical framework by extending the DFN model with a multi-scale mechanical sub-model that captures both concentration-driven and interaction-driven stress contributions at the particle and electrode scales, enabling systematic exploration of stress-electrochemistry coupling across a broad range of operating conditions and cell designs.

The model simulates EIS, DRT, and ICA, demonstrating for the first time how mechanical stress modifies lithium-ion cell electrochemical responses. Results show stress systematically shifts ICA peaks to lower voltages via hydrostatic stress reducing lithium chemical potentials through Gibbs free energy contributions, with direction governed by dominant electrode. EIS and DRT simulations further reveal that at fixed voltage, stress adjusts particle stoichiometry, yielding SoC-dependent charge-transfer resistance changes (decreasing at low SoC, increasing at high SoC) and corresponding DRT peak variations via exchange current density shifts.

For the first time, these effects are explained through basic thermodynamics – stress perturbs reaction equilibria, driving voltage or stoichiometry shifts for energy minimization – thus resolving literature discrepancies arising from material-dependent electrode dominance or SoC variations.

Collectively, these findings highlight the importance of incorporating mechanics into physics-based battery models and establish a foundation for stress-aware diagnostic and prognostic tools in advanced energy storage systems.

CRediT authorship contribution statement

Jasmina Tabaković: Writing – original draft, Visualization, Validation, Software, Methodology, Investigation, Formal analysis, Data curation, Conceptualization. **Tomaž Katrašnik:** Writing – review & editing, Supervision, Resources, Project administration, Investigation, Funding acquisition, Conceptualization. **Klemen Zelič:** Writing – review & editing, Writing – original draft, Supervision, Methodology, Investigation, Formal analysis, Conceptualization.

Declaration of competing interest

The authors declare the following financial interests/personal relationships which may be considered as potential competing interests: Tomaz Katrasnik reports financial support was provided by Horizon 2020 European Innovation Council Fast Track to Innovation. Tomaz Katrasnik reports financial support was provided by Austrian Research Promotion Agency. Tomaz Katrasnik reports financial support was provided by Slovenian Research and Innovation Agency. If there are other authors, they declare that they have no known competing financial interests or personal relationships that could have appeared to influence the work reported in this paper.

Acknowledgments

The authors acknowledge support from the European Union's Horizon 2020 research and innovation programme under Grant Agreement No. 101069910 (NEXTCELL), No. 101069743 (ADVAGEN), No. 101103755 (FASTEST), No. 101103898 (NEXTBMS) and No. 101069686 (PULSELiON). The authors also acknowledge financial support from the Austrian Research Promotion Agency (FFG, project MoSiLIB, No. FO999891450) and the Slovenian Research and Innovation Agency (research core funding No. P2-0401 and project GC-0004).

Appendix A. Computation of ICA, EIS, and DRT from the simulated voltage response

A.1. Incremental capacity analysis

The instantaneous capacity is obtained by integrating the applied current over time,

$$Q(t) = \int_0^t I(t)\,dt, \tag{A.1}$$

where $I(t)$ is the (dis)charge current applied at C/100. The incremental capacity is then computed from the simulated voltage response $V(t)$ using the chain rule,

$$\frac{dQ}{dV} = \frac{dQ/dt}{dV/dt} = \frac{I(t)}{dV/dt}, \tag{A.2}$$

and the resulting curve is smoothed with a Savitzky–Golay filter [62] before being plotted as a function of V.

A.2. Electrochemical impedance spectroscopy

For each excitation frequency f (angular frequency $\omega = 2\pi f$), a sinusoidal current perturbation was applied to the coupled electrochemical–mechanical model around the operating point,

$$I(t) = I_0 + \Delta I \sin(\omega t), \tag{A.3}$$

and the simulated voltage response was fitted, after discarding the initial transient cycles, to a sinusoidal function of the same frequency,

$$V(t) = V_0 + \Delta V \sin(\omega t + \varphi), \tag{A.4}$$

where V_0 is the mean voltage, ΔV the response amplitude, and φ the phase shift relative to the current perturbation. The complex impedance at frequency ω is then obtained from the fitted amplitude ratio and phase shift as

$$Z(\omega) = \frac{\Delta V}{\Delta I}\, e^{i\varphi} = \mathrm{Re}\{Z(\omega)\} + i\,\mathrm{Im}\{Z(\omega)\}, \tag{A.5}$$

with real and imaginary parts

$$\mathrm{Re}\{Z(\omega)\} = \frac{\Delta V}{\Delta I}\cos\varphi, \qquad \mathrm{Im}\{Z(\omega)\} = \frac{\Delta V}{\Delta I}\sin\varphi, \tag{A.6}$$

magnitude $|Z(\omega)| = \Delta V/\Delta I$, and phase angle $\varphi(\omega)$. Repeating this procedure over the logarithmically spaced frequency set yields the frequency-dependent spectrum $Z(\omega)$ reported in the Nyquist plots.

A.3. Distribution of relaxation times

The DRT model represents the impedance spectrum obtained from Eq. (A.5) as a continuous superposition of parallel resistor–capacitor (Voigt) elements,

$$Z(f) = R_\infty + \int_0^\infty \frac{g(\tau)}{1 + i2\pi f\tau}\,d\tau, \tag{A.7}$$

where f is the excitation frequency, R_∞ is the Ohmic resistance, τ the relaxation time, and $g(\tau)$, the (unknown) distribution of relaxation times. Recovering $g(\ln\tau)$ from $Z(f)$ constitutes an ill-posed Fredholm integral equation of the first kind. In this work, the deconvolution was performed with the commercial RelaxIS software [63], based on the framework of the Ciucci group [64], in which $g(\ln\tau)$ is discretized using radial basis functions (RBFs) rather than discrete Voigt elements, yielding the linear model $Z(f_n) = R_\infty + (A'x)_n + i(A''x)_n$, and the resulting regularized least-squares problem is solved via Tikhonov regularization,

$$x_{\mathrm{opt}} = \arg\min_x \left(\left\| A'x - Z'_{\mathrm{exp}} \right\|_2^2 + \left\| A''x - Z''_{\mathrm{exp}} \right\|_2^2 + \lambda \left\| Lx \right\|_2^2 \right), \tag{A.8}$$

where x is the vector of RBF weights approximating $g(\ln\tau)$, A' and A'' are the discretization matrices for the real and imaginary parts of Eq. (A.7), Z'_{exp} and Z''_{exp} are the measured real and imaginary impedance components, L is the Cholesky factor of the derivative-penalty matrix ($M = L^\top L$), and λ is the regularization parameter. For full derivation please see [64].

Appendix B. Derivation of the stress-dependent charge-transfer kinetics

The derivation follows Wu et al. [15] and Le et al. [65], and is reproduced here for completeness. The lithium intercalation reaction proceeds via the exchange of lithium between an electrolyte ion and a vacant intercalation site in the solid,

$$\mathrm{Li}^+ + \mathrm{e}^- + \Theta \rightleftharpoons \mathrm{Li}\text{-}\Theta, \tag{B.1}$$

where Θ denotes an interstitial site. Following transition-state theory, the forward and backward reaction rates are

$$r_{\rightarrow} = r_0 \exp\left(-\frac{\mu_{TS} - \mu_{\mathrm{Li}\text{-}\Theta}}{R_{\mathrm{g}}T}\right), \qquad r_{\leftarrow} = r_0 \exp\left(-\frac{\mu_{TS} - (\mu_{\mathrm{Li}^+} + \mu_{e^-} + \mu_\Theta)}{R_{\mathrm{g}}T}\right), \tag{B.2}$$

where r_0 is a rate constant, μ_{TS} the transition-state chemical potential and μ_i the chemical potential of species i. In the stress-free state these are

$$\begin{aligned} \mu_{\mathrm{Li}\text{-}\Theta} &= \mu^0_{\mathrm{Li}\text{-}\Theta} + R_{\mathrm{g}}T\ln a_{\mathrm{Li}\text{-}\Theta}, & \mu_{\mathrm{Li}^+} &= \mu^0_{\mathrm{Li}^+} + R_{\mathrm{g}}T\ln a_{\mathrm{Li}^+} + F\varphi_{\mathrm{e}}, \\ \mu_\Theta &= \mu^0_\Theta + R_{\mathrm{g}}T\ln a_\Theta, & \mu_{e^-} &= -F\varphi_{\mathrm{s}}, \end{aligned} \tag{B.3}$$

where a_i is the activity of species i, and φ_{e} and φ_{s} are the local electrolyte and solid electric potentials, both referred to a common reference point.

Under mechanical stress, the chemical potentials of the electrolyte ion and the electron are unaffected, whereas the two solid-phase species acquire an additional stress contribution, in analogy to Eq. (40):

$$\mu_{\mathrm{Li}\text{-}\Theta} = \mu^0_{\mathrm{Li}\text{-}\Theta} + R_{\mathrm{g}}T\ln a_{\mathrm{Li}\text{-}\Theta} - \Omega_{\mathrm{Li}\text{-}\Theta}\sigma_{\mathrm{h}}, \qquad \mu_\Theta = \mu^0_\Theta + R_{\mathrm{g}}T\ln a_\Theta - \Omega_\Theta\sigma_{\mathrm{h}}, \tag{B.4}$$

with $\Omega = \Omega_{\mathrm{Li}\text{-}\Theta} - \Omega_\Theta$ the net partial molar volume of lithium in the solid. The transition-state potential is correspondingly split between the two reaction pathways by a mechanical symmetry factor α_{m}, in analogy to the electrochemical symmetry factor α:

$$\mu_{TS} = \mu^0_{TS} + (1-\alpha)F(\varphi_{\mathrm{e}} - \varphi_{\mathrm{s}}) + \alpha_{\mathrm{m}}\left(-\Omega_{\mathrm{Li}\text{-}\Theta}\sigma_{\mathrm{h}}\right) + (1-\alpha_{\mathrm{m}})\left(-\Omega_\Theta\sigma_{\mathrm{h}}\right). \tag{B.5}$$

Substituting Eqs. (B.4)–(B.5) into Eq. (B.2) and collecting the standard-state contributions into the anodic and cathodic rate constants,

$$k_{\mathrm{a}} = r_0 \exp\left(-\frac{\mu^0_{TS} - \mu^0_{\mathrm{Li}\text{-}\Theta}}{R_{\mathrm{g}}T}\right), \qquad k_{\mathrm{c}} = r_0 \exp\left(-\frac{\mu^0_{TS} - \mu^0_\Theta - \mu^0_{\mathrm{Li}^+}}{R_{\mathrm{g}}T}\right), \tag{B.6}$$

yields the net reaction rate

$$\begin{aligned} r = r_{\rightarrow} - r_{\leftarrow} = {} & k_{\mathrm{a}} a_{\mathrm{Li}\text{-}\Theta} \exp\left[\frac{(1-\alpha)F(\varphi_{\mathrm{s}} - \varphi_{\mathrm{e}})}{R_{\mathrm{g}}T} - \frac{(1-\alpha_{\mathrm{m}})\Omega\sigma_{\mathrm{h}}}{R_{\mathrm{g}}T}\right] \\ & - k_{\mathrm{c}} a_{\mathrm{Li}^+} a_\Theta \exp\left[-\frac{\alpha F(\varphi_{\mathrm{s}} - \varphi_{\mathrm{e}})}{R_{\mathrm{g}}T} + \frac{\alpha_{\mathrm{m}}\Omega\sigma_{\mathrm{h}}}{R_{\mathrm{g}}T}\right]. \end{aligned} \tag{B.7}$$

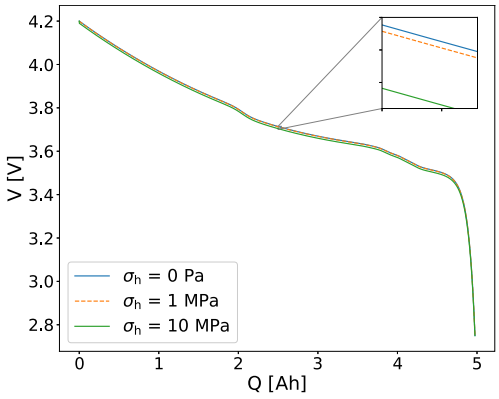

Fig. C.5. Quasi-equilibrium discharge profiles of the NMC/graphite cell at a C/1000 rate under different hydrostatic stress levels, highlighting the influence of external mechanical loading on the full-cell voltage.

The condition $r = 0$ defines the stress-modified equilibrium potential U_m,

$$(\varphi_s - \varphi_e)_{eq} = U_m = \frac{R_g T}{F} \ln\left(\frac{k_c}{k_a}\right) + \frac{R_g T}{F} \ln\left(\frac{a_{Li^+} a_\Theta}{a_{Li\text{-}\Theta}}\right) + \frac{\Omega \sigma_h}{F}, \tag{B.8}$$

in which the first two terms reproduce the stress-free equilibrium potential U and the third represents the purely mechanical shift. Referring the potentials to a lithium metal reference electrode, for which $\Phi_s = \varphi_s$ and $\Phi_e = \varphi_e + \left(\mu^0_{Li^+} + R_g T \ln a_{Li^+} - \mu^0_{Li}\right)/F$, eliminates the electrolyte activity and replaces U by the concentration-dependent open-circuit potential $E_{ref}(c_{s,surf})$, so that

$$U_m \longrightarrow E_{ref}(c_{s,surf}) + \frac{\Omega\, \sigma_{h,surf}}{F}. \tag{B.9}$$

The overpotential including the mechanical contribution therefore becomes

$$\eta_m = \varphi_s - \varphi_e - U_m = \Phi_s - \Phi_e - E_{ref}(c_{s,surf}) - \frac{\Omega\, \sigma_{h,surf}}{F}, \tag{B.10}$$

which recovers Eq. (41). Finally, substituting Eq. (B.8) back into Eq. (B.7) and expressing the result in terms of η_m gives an identical mechanical prefactor in both the anodic and the cathodic branch, since $(1-\alpha) - (1-\alpha_m) = \alpha_m - \alpha$ and $\alpha_m - \alpha$, respectively:

$$i = rF = j_0 \exp\left[\frac{(\alpha_m - \alpha)\, \Omega \sigma_{h,surf}}{R_g T}\right] \left[\exp\left(\frac{F(1-\alpha)}{R_g T}\eta_m\right) - \exp\left(-\frac{F\alpha}{R_g T}\eta_m\right)\right], \tag{B.11}$$

with the stress-free exchange current density $j_0 = F\left(k_a a_{Li\text{-}\Theta}\right)^{\alpha}\left(k_c a_{Li^+} a_\Theta\right)^{1-\alpha}$. With the sign convention $J = -i/F$ adopted for the pore-wall molar flux in Table 1, Eq. (B.11) is identical to Eq. (42). Mechanical stress thus enters the kinetics in two distinct ways, as a scaling of the exchange current density and as a shift of the equilibrium potential.

Appendix C. Discharge profiles and internal state spatial profiles of the NMC/graphite cell under hydrostatic stress

See Figs. C.5 and C.6.

Appendix D. Parametric sensitivity study

The parametric sensitivity study presented in this appendix uses the same baseline electrochemical and mechanical parameters as the main simulations (Table 3), varying only one parameter at a time while holding all others fixed at their baseline values. This one-at-a-time (OAT) design isolates the individual effect of each parameter on the electrode-dominance behavior and the resulting ICA, EIS, and DRT signatures, without confounding the effects of multiple simultaneously varying properties (see Fig. D.7).Table D.4 summarizes the perturbed value tested for each parameter, relative to the baseline values given in Table 3. The partial molar volume (Ω) was varied independently for each electrode to test electrode dominance: first increased on the cathode side, and separately increased on the anode side, such that the previously non-dominant electrode became dominant and the direction of the full-cell trends reversed. The equilibrium diffusion coefficient (D_{eq}) was varied by a factor of ten above and below its baseline value, for the cathode and anode independently. The cathode open-circuit potential (OCP) slope was varied by substituting values representative of an LFP-like chemistry and a logarithmic mean between NMC and LFP, to probe the sensitivity of electrode dominance to the solid-solution versus phase-separating character of the cathode chemistry; the anode (graphite) OCP slope was held fixed at its baseline value in all cases.

Appendix E. Effect of applied pressure on cathode surface concentration

See Fig. E.9.

Appendix F. Consistency between DRT peak areas and EIS-derived charge-transfer resistance

Since Peaks 1 and 2 of the distribution of relaxation times (DRT) are not individually resolvable as separate semicircles in the raw Nyquist spectrum, their physical validity was assessed by comparing their summed area against the charge-transfer resistance obtained directly from the impedance data. The area under each DRT peak, $R_{peak,i} = \int_{\ln \tau_{i,1}}^{\ln \tau_{i,2}} \gamma(\ln \tau)\, d(\ln \tau)$, was computed by trapezoidal integration of $\gamma(\tau)$ over $\ln \tau$, with peak boundaries $\tau_{i,1}, \tau_{i,2}$ identified from the DRT spectrum. The corresponding EIS-derived resistance, R_{ct}^{EIS}, was obtained as the span of $\mathrm{Re}(Z)$ between the high- and low-frequency limits of the merged charge-transfer arc, excluding the high-frequency inductive artifact and the low-frequency diffusion tail associated with the third (artifactual) DRT peak. Table F.5 reports this comparison for all simulated stress levels and battery voltages. It can be seen, that the relative difference remains below 0.5% in all cases, confirming that the two peaks resolved by DRT jointly reproduce the resistance directly measurable from the impedance spectrum.

Data availability

Data will be made available on request.

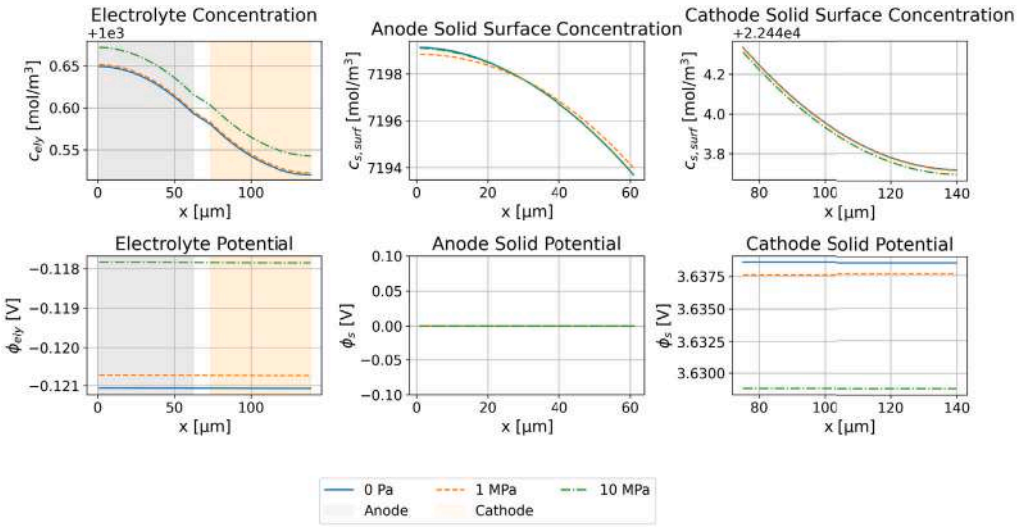

Fig. C.6. Pressure-induced changes in the internal state of the NMC/graphite cell at 3.64 V, showing electrolyte concentration and potential, together with solid surface concentration and solid potential.

Table D.4
Perturbed parameter values used in the one-at-a-time parametric sensitivity study. Case labels correspond to the subfigures in Fig. D.7.

Case	Parameter	Electrode	Perturbed value
(a)	Ω [m^3/mol]	Cathode (p)	3.75×10^{-5}
(b)	Ω [m^3/mol]	Anode (n)	1.705×10^{-5}
(c)	D_{eq} [m^2/s]	Cathode (p)	8×10^{-14}
(d)	D_{eq} [m^2/s]	Anode (n)	5×10^{-14}
(e)	OCP slope	Cathode (LFP-like)	−2.07%
(f)	OCP slope	Cathode (log. mean)	−10.83%

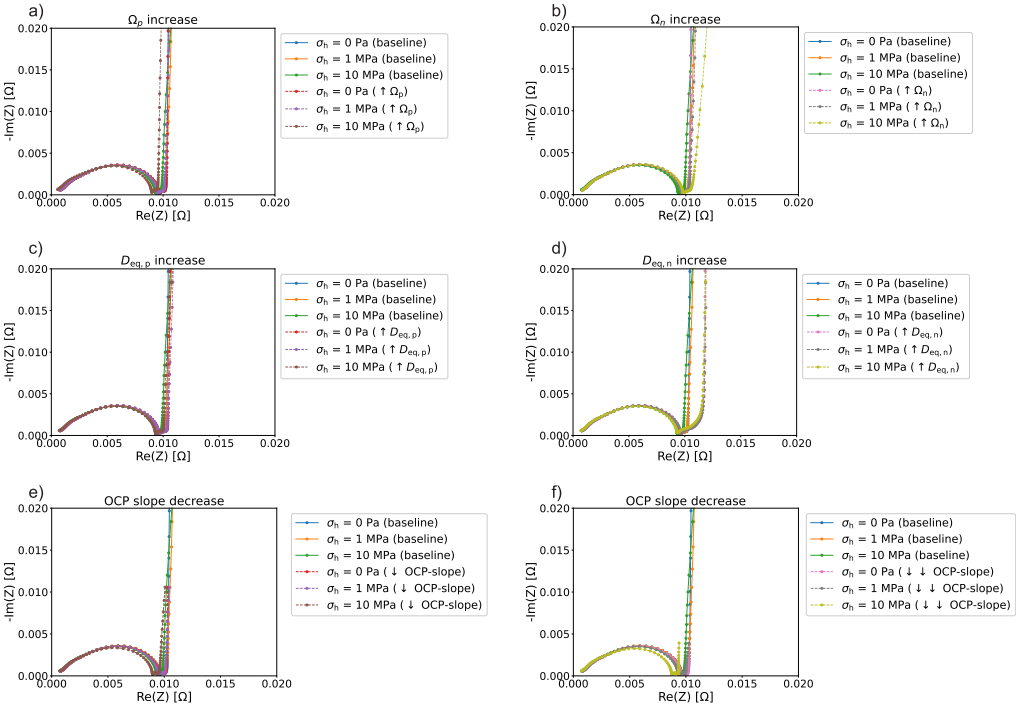

Fig. D.7. Sensitivity of the simulated impedance response at 3.64 V to the partial molar volume (Ω), equilibrium diffusion coefficient (D_{eq}), and cathode OCP slope. Ω was varied independently for the cathode and the anode (panels a, b) and D_{eq} was varied independently for the cathode and the anode (panels c, d) to test electrode dominance, while the cathode OCP slope was reduced (panels e, f) to mimic the LFP plateau slope and intermediate slope to assess the generalizability of the observed pressure-dependent trends across cell chemistries.

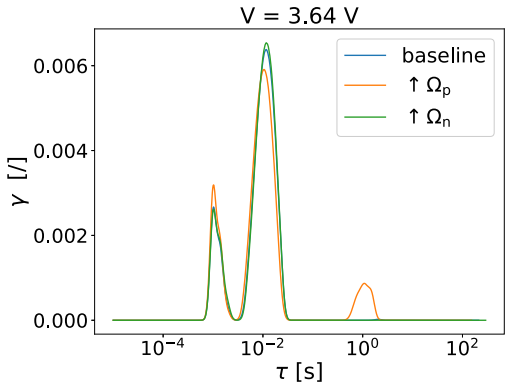

Fig. D.8. Sensitivity of the DRT spectrum to electrode-specific partial molar volume. Increasing the cathode partial molar volume Ω_p selectively increases Peak 1, while increasing the anode partial molar volume Ω_n selectively increases Peak 2.

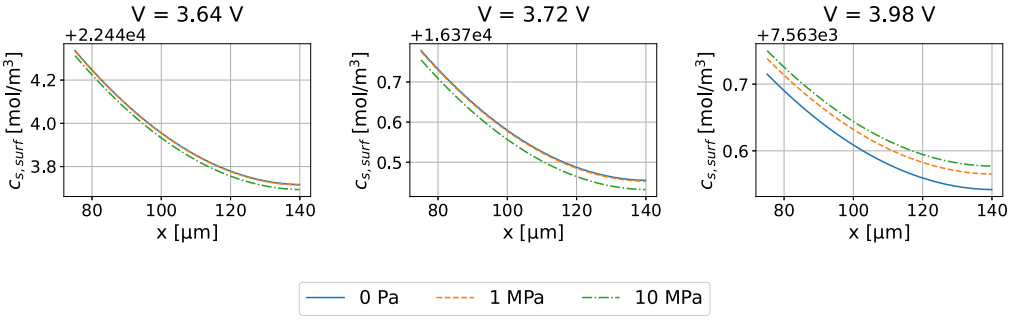

Fig. E.9. Cathode solid surface concentration profiles along the electrode thickness at three states of charge under applied mechanical stress of 0 Pa, 1 MPa, and 10 MPa.

Table F.5
Comparison of the summed DRT peak 1 and peak 2 areas against the EIS-derived charge-transfer resistance, for all simulated stress levels and battery voltages.

V [V]	σ_h [MPa]	R_{peak1} [mΩ]	R_{peak2} [mΩ]	$R_{\text{ct}}^{\text{DRT}}$ [mΩ]	$R_{\text{ct}}^{\text{EIS}}$ [mΩ]	Rel. diff. [%]
3.64	0	1.61	7.14	8.75	8.78	−0.30
	1	1.60	7.14	8.74	8.75	−0.12
	10	1.66	6.94	8.60	8.59	+0.16
3.72	0	1.55	6.34	7.89	7.89	−0.05
	1	1.55	6.37	7.91	7.90	+0.16
	10	1.62	6.37	7.98	7.95	+0.46
3.98	0	1.51	7.07	8.58	8.58	−0.06
	1	1.50	7.10	8.61	8.60	+0.10
	10	1.55	7.19	8.75	8.72	+0.27

References

[1] S. Atlung, K. West, T. Jacobsen, Dynamic aspects of solid solution cathodes for electrochemical power sources, J. Electrochem. Soc. 126 (8) (1979) 1311.

[2] M. Doyle, T.F. Fuller, J. Newman, Modeling of galvanostatic charge and discharge of the lithium/polymer/insertion cell, J. Electrochem. Soc. 140 (6) (1993) 1526, http://dx.doi.org/10.1149/1.2221597.

[3] S.G. Marquis, V. Sulzer, R. Timms, C.P. Please, S.J. Chapman, An asymptotic derivation of a single particle model with electrolyte, J. Electrochem. Soc. 166 (15) (2019) A3693, http://dx.doi.org/10.1149/2.0341915jes.

[4] I. Mele, K. Zelič, M. Firm, J. Moškon, M.G. cek, T. Katrašnik, Enhanced porous electrode theory based electrochemical model for higher fidelity modelling and deciphering of the EIS spectra, J. Electrochem. Soc. 171 (8) (2024) 080537, http://dx.doi.org/10.1149/1945-7111/ad6eb9.

[5] V.S. Deshpande, R.M. McMeeking, Models for the interplay of mechanics, electrochemistry, thermodynamics, and kinetics in lithium-ion batteries, Appl. Mech. Rev. 75 (1) (2023) 010801, http://dx.doi.org/10.1115/1.4056289, arXiv:https://asmedigitalcollection.asme.org/appliedmechanicsreviews/article-pdf/75/1/010801/6974782/amr_075_01_010801.pdf.

[6] J.S. Edge, S. O'Kane, R. Prosser, N.D. Kirkaldy, A.N. Patel, A. Hales, A. Ghosh, W. Ai, J. Chen, J. Yang, S. Li, M.-C. Pang, L.B. Diaz, A. Tomaszewska, M.W. Marzook, K.N. Radhakrishnan, H. Wang, Y. Patel, B. Wu, G.J. Offer, Lithium ion battery degradation: what you need to know, Phys. Chem. Chem. Phys. 23 (2021) 8200–8221, http://dx.doi.org/10.1039/D1CP00359C.

[7] M. Ebner, F. Marone, M. Stampanoni, V. Wood, Visualization and quantification of electrochemical and mechanical degradation in li ion batteries, Science 342 (6159) (2013) 716–720, http://dx.doi.org/10.1126/science.1241882, URL https://www.science.org/doi/abs/10.1126/science.1241882.

[8] R. Xu, Y. Yang, F. Yin, P. Liu, P. Cloetens, Y. Liu, F. Lin, K. Zhao, Heterogeneous damage in Li-ion batteries: Experimental analysis and theoretical modeling, J. Mech. Phys. Solids 129 (2019) 160–183, http://dx.doi.org/10.1016/j.jmps.2019.05.003, URL https://www.sciencedirect.com/science/article/pii/S0022509619303126.

[9] X. Zhang, W. Shyy, A. Marie Sastry, Numerical simulation of intercalation-induced stress in Li-ion battery electrode particles, J. Electrochem. Soc. 154 (10) (2007) A910, http://dx.doi.org/10.1149/1.2759840.

[10] J. Christensen, J. Newman, A mathematical model of stress generation and fracture in lithium manganese oxide, J. Electrochem. Soc. 153 (6) (2006) A1019, http://dx.doi.org/10.1149/1.2185287.

[11] R. Xu, L.S. de Vasconcelos, K. Zhao, Computational analysis of chemomechanical behaviors of composite electrodes in Li-ion batteries, J. Mater. Res. 31 (18) (2016) 2715–2727, http://dx.doi.org/10.1557/jmr.2016.302.

[12] R. Xu, K. Zhao, Mechanical interactions regulated kinetics and morphology of composite electrodes in Li-ion batteries, Extrem. Mech. Lett. 8 (2016) 13–21.

[13] H. Mendoza, S.A. Roberts, V.E. Brunini, A.M. Grillet, Mechanical and electrochemical response of a LiCoO2 cathode using reconstructed microstructures, Electrochim. Acta 190 (2016) 1–15.

[14] S.A. Roberts, V.E. Brunini, K.N. Long, A.M. Grillet, A framework for three-dimensional mesoscale modeling of anisotropic swelling and mechanical deformation in lithium-ion electrodes, J. Electrochem. Soc. 161 (11) (2014) F3052.

[15] B. Wu, W. Lu, A consistently coupled multiscale mechanical–electrochemical battery model with particle interaction and its validation, J. Mech. Phys. Solids 125 (2019) 89–111, http://dx.doi.org/10.1016/j.jmps.2018.12.005, URL https://www.sciencedirect.com/science/article/pii/S0022509618309141.

[16] M. Gaberšček, Understanding Li-based battery materials via electrochemical impedance spectroscopy, Nat. Commun. 12 (2021) 6513, http://dx.doi.org/10.1038/s41467-021-26894-5.

[17] C. Plank, T. Rüther, L. Jahn, M. Schamel, J.P. Schmidt, F. Ciucci, M.A. Danzer, A review on the distribution of relaxation times analysis: A powerful tool for process identification of electrochemical systems, J. Power Sources 594 (2024) 233845.

[18] J.P. Schmidt, T. Chrobak, M. Ender, J. Illig, D. Klotz, E. Ivers-Tiffée, Studies on LiFePO4 as cathode material using impedance spectroscopy, J. Power Sources 196 (12) (2011) 5342–5348.

[19] N. Lyu, Y. Jin, R. Xiong, S. Miao, J. Gao, Real-time overcharge warning and early thermal runaway prediction of Li-ion battery by online impedance measurement, IEEE Trans. Ind. Electron. 69 (2) (2021) 1929–1936.

[20] Y. Zhao, V. Kumtepeli, S. Ludwig, A. Jossen, Investigation of the distribution of relaxation times of a porous electrode using a physics-based impedance model, J. Power Sources 530 (2022) 231250.

[21] O.B. Saban, M.A. Arslan, M.F. Serincan, Multiphysics modeling of lithium-ion batteries: a novel DRT-enhanced electro-thermal framework, Ionics 31 (10) (2025) 10327–10351.

[22] L. Wang, X. Zhao, Z. Deng, L. Yang, Application of electrochemical impedance spectroscopy in battery management system: State of charge estimation for aging batteries, J. Energy Storage 57 (2023) 106275.

[23] M. Galeotti, L. Cinà, C. Giammanco, S. Cordiner, A. Di Carlo, Performance analysis and SOH (state of health) evaluation of lithium polymer batteries through electrochemical impedance spectroscopy, Energy 89 (2015) 678–686.

[24] Y. Cui, P. Zuo, C. Du, Y. Gao, J. Yang, X. Cheng, Y. Ma, G. Yin, State of health diagnosis model for lithium ion batteries based on real-time impedance and open circuit voltage parameters identification method, Energy 144 (2018) 647–656.

[25] A.S. Akram, M. Sohaib, W. Choi, SOH estimation of lithium-ion batteries using distribution of relaxation times parameters and long short-term memory model, Batteries 11 (5) (2025) 183.

[26] D. Jiang, Y. Zhang, Z. Gao, Z. Zhang, S. Li, Y. Jin, J. Liu, H. Wang, Single frequency feature point derived from DRT for SOH estimation of lithium ion battery, J. Electrochem. Soc. 172 (3) (2025) 030514.

[27] J. Wen, X. Chen, X. Li, Y. Li, SOH prediction of lithium battery based on IC curve feature and BP neural network, Energy 261 (2022) 125234.

[28] H. Sun, J. Sun, K. Zhao, L. Wang, K. Wang, Data-driven ICA-Bi-LSTM-combined lithium battery SOH estimation, Math. Probl. Eng. 2022 (1) (2022) 9645892.

[29] P. Iurilli, C. Brivio, V. Wood, On the use of electrochemical impedance spectroscopy to characterize and model the aging phenomena of lithium-ion batteries: a critical review, J. Power Sources 505 (2021) 229860.

[30] R. Xiong, J. Tian, H. Mu, C. Wang, A systematic model-based degradation behavior recognition and health monitoring method for lithium-ion batteries, Appl. Energy 207 (2017) 372–383.

[31] X. Zhu, H. Wang, S. Allu, Y. Gao, E. Cakmak, E.J. Hopkins, G.M. Veith, Z. Wang, Investigation on capacity loss mechanisms of lithium-ion pouch cells under mechanical indentation conditions, J. Power Sources 465 (2020) 228314.

[32] P. Iurilli, C. Brivio, V. Wood, Detection of lithium-ion cells' degradation through deconvolution of electrochemical impedance spectroscopy with distribution of relaxation time, Energy Technol. 10 (10) (2022) 2200547.

[33] D. Anseán, V.M. García, M. González, C. Blanco-Viejo, J.C. Viera, Y.F. Pulido, L. Sánchez, Lithium-ion battery degradation indicators via incremental capacity analysis, IEEE Trans. Ind. Appl. 55 (3) (2019) 2992–3002.

[34] X. Cai, C. Zhang, Z. Chen, L. Zhang, D.U. Sauer, W. Li, Characterization and quantification of multi-field coupling in lithium-ion batteries under mechanical constraints, J. Energy Chem. 95 (2024) 364–379, http://dx.doi.org/10.1016/j.jechem.2024.03.048, URL https://www.sciencedirect.com/science/article/pii/S2095495624002602. Dostopano: 17.07.2025.

[35] A. Barai, R. Tangirala, K. Uddin, J. Chevalier, Y. Guo, A. McGordon, P. Jennings, The effect of external compressive loads on the cycle lifetime of lithium-ion pouch cells, J. Energy Storage 13 (2017) 211–219.

[36] M. Li, Y. Hu, C. Lu, B. Li, W. Tian, J. Zhang, Z. Mao, Effect of hydrostatic pressure on electrochemical performance of soft package lithium-ion battery for autonomous underwater vehicles, J. Energy Storage 54 (2022) 105325.

[37] X. Peng, J. Han, Q. Zhang, Y. Xiang, X. Hu, Real-time mechanical and thermal monitoring of lithium batteries with PVDF-trfe thin films integrated within the battery, Sensors Actuators A: Phys. 338 (2022) 113484.

[38] W. Jiao, M. Zohair, J. Eaves-Rathert, J. Ramamurthy, A. Harkaway, R. Mort, J. Wheaton, S. Jiang, S.W. Martin, C.L. Pint, Critical role of pressure for chemo-mechanical-induced stability of sodium metal battery anodes, ACS Energy Lett. 8 (6) (2023) 2711–2717.

[39] X. Du, Y. Hu, S.-Y. Choe, T.R. Garrick, M.A. Fernandez, Characterization and analysis of the effect of pressure on the performance of a large format NMC/C lithium-ion battery, J. Power Sources 573 (2023) 233117, http://dx.doi.org/10.1016/j.jpowsour.2023.233117, URL https://www.sciencedirect.com/science/article/pii/S0378775323004925.

[40] V. Müller, V. Küpers, J. Schmalz, S. Dörfler, N. Löffler, A.J. Smith, A. Latz, M. Wohlfahrt-Mehrens, Study of the influence of mechanical pressure on the performance and aging of lithium-ion battery cells, J. Power Sources 440 (2019) 227148, http://dx.doi.org/10.1016/j.jpowsour.2019.227148, URL https://www.sciencedirect.com/science/article/pii/S0378775319311413.

[41] P. Daubinger, F. Ebert, S. Hartmann, G.A. Giffin, Impact of electrochemical and mechanical interactions on lithium-ion battery performance investigated by operando dilatometry, J. Power Sources 488 (2021) 229457.

[42] A.S. Mussa, M. Klett, G. Lindbergh, R.W. Lindström, Effects of external pressure on the performance and ageing of single-layer lithium-ion pouch cells, J. Power Sources 385 (2018) 18–26.

[43] A. Barai, Y. Guo, A. McGordon, P. Jennings, A study of the effects of external pressure on the electrical performance of a lithium-ion pouch cell, in: 2013 International Conference on Connected Vehicles and Expo, ICCVE, IEEE, 2013, pp. 295–299.

[44] C. Drießen, E. Michelini, J. Moser, P. Höschele, Sensitivity of electrochemical impedance parameters for detecting changes in lithium-ion batteries due to acceleration shocks and local mechanical deformations, J. Power Sources 648 (2025) 237308, http://dx.doi.org/10.1016/j.jpowsour.2025.237308, URL https://www.sciencedirect.com/science/article/pii/S0378775325011449.

[45] J.-M. Doux, Y. Yang, D.H. Tan, H. Nguyen, E.A. Wu, X. Wang, A. Banerjee, Y.S. Meng, Pressure effects on sulfide electrolytes for all solid-state batteries, J. Mater. Chem. A 8 (10) (2020) 5049–5055.

[46] D. Sauerteig, N. Hanselmann, A. Arzberger, H. Reinshagen, S. Ivanov, A. Bund, Electrochemical-mechanical coupled modeling and parameterization of swelling and ionic transport in lithium-ion batteries, J. Power Sources 378 (2018) 235–247.

[47] D. Lee, Y. Kim, M. Shin, The role of stack pressure in modulating electrochemical behavior of all-solid-state lithium–sulfur batteries, Korean J. Chem. Eng. (2025) 1–9.

[48] F. Yang, Q. Xu, X. Qin, L. Zhao, L. Guo, Y. Zhang, D. Kong, J. Han, L. Zhi, Mechanical influence mechanisms of silicon anodes in solid-state batteries under low stack pressure, J. Power Sources 652 (2025) 237634.

[49] I.A. Shozib, F.D. Cúñez, M. Ganter, A. Leggiero, R. Liu, Q.H. Tu, Interplay of interfacial adhesion and mechanical degradation in anode-free solid-state batteries, J. Electrochem. Soc. 171 (9) (2024) 090524.

[50] F. Zhang, Z. Cai, R. Liu, Y. Sun, H. Pan, Guiding uniform Zn electrodeposition through regulating pressure for stable aqueous Zn batteries, J. Mater. Chem. A 12 (17) (2024) 10341–10348.

[51] E. Petursdottir, M. Kohlhuber, H. Ehrenberg, Influence from mechanical stress on state of health of large prismatic lithium-ion-cells under various temperatures, J. Electrochem. Soc. 171 (7) (2024) 070510.

[52] N.A. Samad, Y. Kim, J.B. Siegel, A.G. Stefanopoulou, Battery capacity fading estimation using a force-based incremental capacity analysis, J. Electrochem. Soc. 163 (8) (2016) A1584.

[53] V. Sulzer, S.G. Marquis, R. Timms, M. Robinson, S.J. Chapman, Python battery mathematical modelling (PyBaMM), J. Open Res. Softw. 9 (1) (2021) 14, http://dx.doi.org/10.5334/jors.309.

[54] J.L. Chu, S. Lee, The effect of chemical stresses on diffusion, J. Appl. Phys. 75 (6) (1994) 2823–2829, http://dx.doi.org/10.1063/1.356174.

[55] E. Bohn, T. Eckl, M. Kamlah, R. McMeeking, A model for lithium diffusion and stress generation in an intercalation storage particle with phase change, J. Electrochem. Soc. 160 (10) (2013) A1638.

[56] T.H. Wan, F. Ciucci, Continuum level transport and electro-chemo-mechanics coupling—solid oxide fuel cells and lithium ion batteries, Electro-Chemo-Mechanics Solids (2017) 161–189.

[57] P. Mohtat, S. Lee, V. Sulzer, J.B. Siegel, A.G. Stefanopoulou, Differential expansion and voltage model for li-ion batteries at practical charging rates, J. Electrochem. Soc. 167 (11) (2020) 110561.

[58] E.J. Cheng, K.H. Wagner, R. Yazami, Y.-M. Chiang, Mechanical and physical properties of LiNi0.33Mn0.33Co0.33O2 (NMC), J. Eur. Ceram. Soc. 37 (9) (2017) 3213–3217, http://dx.doi.org/10.1016/j.jeurceramsoc.2017.03.048.

[59] I. Laresgoiti, S. Käbitz, M. Ecker, D.U. Sauer, Modeling mechanical degradation in lithium ion batteries during cycling: Solid electrolyte interphase fracture, J. Power Sources 300 (2015) 112–122, http://dx.doi.org/10.1016/j.jpowsour.2015.09.033, URL https://www.sciencedirect.com/science/article/pii/S0378775315302949.

[60] J. Cannarella, C.B. Arnold, Stress evolution and capacity fade in constrained lithium-ion pouch cells, J. Power Sources 245 (2014) 745–751.

[61] S.P. Nadimpalli, V.A. Sethuraman, D.P. Abraham, A.F. Bower, P.R. Guduru, Stress evolution in lithium-ion composite electrodes during electrochemical cycling and resulting internal pressures on the cell casing, J. Electrochem. Soc. 162 (14) (2015) A2656.

[62] SciPy Community, savgol filter - SciPy Reference Manual. URL https://docs.scipy.org/doc/scipy/reference/generated/scipy.signal.savgol_filter.html. Dostopano: 17.07.2025.

[63] rhd instruments GmbH & Co. KG, RelaxIS DRT, 2025, URL https://relaxis-drt.rhd-instruments.de/. Distribution of Relaxation Times (DRT) module; version as of access date.

[64] T.H. Wan, M. Saccoccio, C. Chen, F. Ciucci, et al., Influence of the discretization methods on the distribution of relaxation times deconvolution: Implementing radial basis functions with drttools, Electrochim. Acta 184 (2015) 483–499, http://dx.doi.org/10.1016/j.electacta.2015.09.097.

[65] A.T. Le, X. Bruant, N.T. Phung, F. Ozanam, M. Rosso, L. Guin, Stress dependence of the chemical potential of lithium in a silicon electrode, J. Mech. Phys. Solids 163 (2026) 106421.

[66] T. Rüther, W. Hileman, G.L. Plett, M.S. Trimboli, M.A. Danzer, Demystifying the distribution of relaxation times: A simulation-based investigation into the limits and possibilities of interpretation for lithium-ion batteries, J. Electrochem. Soc. 171 (6) (2024) 060508, http://dx.doi.org/10.1149/1945-7111/ad4fe5.

[67] B. Py, F. Wang, J. Wang, M. Filippone, F. Ciucci, Review of timescale distributions for electrochemical impedance spectroscopy analysis: Advantages, synergies, and future directions, DeCarbon 13 (2026) 100178, http://dx.doi.org/10.1016/j.decarb.2026.100178, URL https://www.sciencedirect.com/science/article/pii/S2949881326000326.